RSC Advances

ROYAL SOCIETY OF CHEMISTRY

www.rsc.org/advances

Cite this: DOI: 10.1039/c0xx00000x

www.rsc.org/xxxxxx

Communication

Bio-inspired directional high-aspect-ratio nanopillars: fabrication and actuation

Weitao Jiang, Lanlan Wang，Hongzhong Liu*，Haoyun Ma, Hongmiao Tian, Bangdao Chen, Yongsheng Shi, Lei Yin, Yucheng Ding

Received (in XXX, XXX) Xth XXXXXXXXX 20XX, Accepted Xth XXXXXXXXX 20XX
DOI: 10.1039/b000000x

Nanopillars (400-500nm in diameter, 20-40 in aspect ratio, and 60°-90° in slanted angles) were fabricated, whose posture can be actuated by electron beam or external electric field.

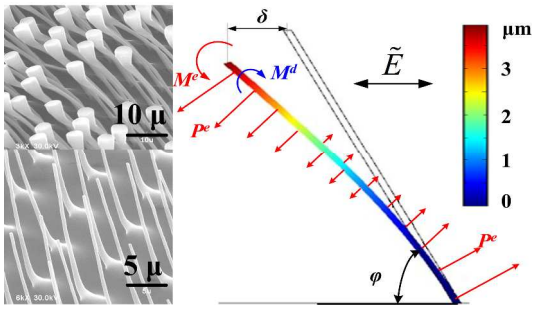

Cite this: DOI: 10.1039/c0xx00000x

www.rsc.org/xxxxxx

Communication

Bio-inspired directional high-aspect-ratio nanopillars: fabrication and actuation

Weitao Jiang, Lanlan Wang，Hongzhong Liu*，Haoyun Ma, Hongmiao Tian, Bangdao Chen, Yongsheng Shi, Lei Yin, Yucheng Ding

Received (in XXX, XXX) Xth XXXXXXXXX 20XX, Accepted Xth XXXXXXXXX 20XX
DOI: 10.1039/b000000x

The Dynamic nature and responsive behaviour are the most attractive features of biological structures, and comprise the goals for next-generation smart materials. The nanostructure arrays provide unique topographic patterns that confer wetting, optical, and many other functions, but their actuation at sub-micrometer scale is still a challenging goal. In this paper, we provide a simple route to fabricate ordered arrays of slender nanopillars with submicron diameter (400-500nm) and high aspect ratio (20-40), with controllable slanted angles (60°-90°). Experiments reveal that, the fabricated slender nanopillars are flexible that their orientation can be dynamically manipulated in response to external electric field, while the stiffness can prevent ground or lateral collapse. The high aspect ratio nanopillars with orientation tunability can find applications in development of smart material, gecko-inspired reversible adhesion, etc.

There is a growing body of information describing natural structures with sophisticated design strategies, which lend the organisms and plants superior mechanical, optical, adhesive, self-cleaning (lotus effect), actuation, and sensing capabilities [1-5]. For example, motile cilia in nature, which can induce movement by constantly beating in a given direction, can fulfil diverse functions ranging from motility to chemical sensing of environmental changes, thus is considered as a promising candidate for microfluidic, bio-mimic and lab-on-a-chip applications. Research on motile-cilia-like micro/nano pillars, based on microfabrication, have achieved significant advances in recent years [6]. The source of stimuli can vary and depends on the material used. A mechanical or chemical response is observed in response to environmental stimuli (pH [7, 8], chemical reaction [9], humidity [10, 11], light [8, 12]) or in response to electrical [6,13]/magnetic [14,15] signals. The common feature of the motile-cilia-like artificial designs is the use of vertical-standing high-aspect-ratio micro/nano structures. Many approaches for various high-aspect-ratio micro/nano structures whose orientation can be actuated were exhibited in previous studies [16-20]. Aizenberg and Sidorenko demonstrated that homogeneous swelling of hydrogel films can lead to an "inhomogeneous" response and the appearance of anisoptropic surface properties. They fabricated thin hydrogel films with incorporated high-aspect-ratio nanorods. Collapse or swelling of the thin hydrogel layer caused change in the orientation of the rods [21].

Even though many stimulus-active polymers or structures have been developed and many applications have been studied in past decades, the research in this area is far from maturity. First, a truly "materials " as well as high-aspect-ratio nanostructures, that themselves responsive to a variety of stimuli and have a finely tuned geometry and stiffness, are desirable. Second, approaches to develop a low-cost procedure to produce an arbitrarily designed micro/nano structures with various stiffness, need to further improve. Third, actuation methods that are compatible to field-by-field driving, rather than environmental driving, deserve further investigation.

In addition, in the plant and animal kingdoms, directional textured surfaces with microscale and nanoscale features provide key functions for survival [22]. All these natural surfaces derive their directional properties from asymmetric micro- or nanostructures such as ratchets or hairy forests. Taking butterfly wing for example, regarding self-cleaning properties, it has been also reported that the butterfly wing exhibits superhydrophobicity (with a water contact angle of 152°) and directional adhesive properties. After a deep investigation, the butterfly wing was found to be covered by microscales overlapped on the wings along the radial outward (RO) direction. Furthermore, the scale surface consists of separate ridging nano-stripes composed of nano-tips stacked stepwise along the RO direction. This interesting phenomenon may offer an insight into the design not only of self-cleaning surfaces but also of smart fluid-controllable interfaces [23]. Inspired by natural directional surfaces, arrays of asymmetric surface features, such as arrays of grooves, inclined pillars, and helical protrusions, have been prepared and impart unique anisotropy in properties including wetting ,adhesion, thermal and/or electrical conductivity, optical activity, and capability to direct cell growth [24]. However, fabrication of asymmetric surface features, as well as directional high-aspect-ratio structures, often pushes the limits of traditional etching and deposition techniques, making it challenging to produce the desired surfaces in a scalable and cost-effective manner.

In this paper, we report a facile strategy to obtain arrays of directional high-aspect-ratio nanopillars, able to undergo reversible, homogeneous, drastic and tunable orientation changes upon application of an electrical field. We demonstrate an effective method for fabrication of high-aspect ratio capped/uncapped nanopillars (400-800nm in diameter and up to

40 in aspect ratio), which can swing in an external electric field (can be easily broadened to field-to-field actuation), with maximum deflection over 10 μm.

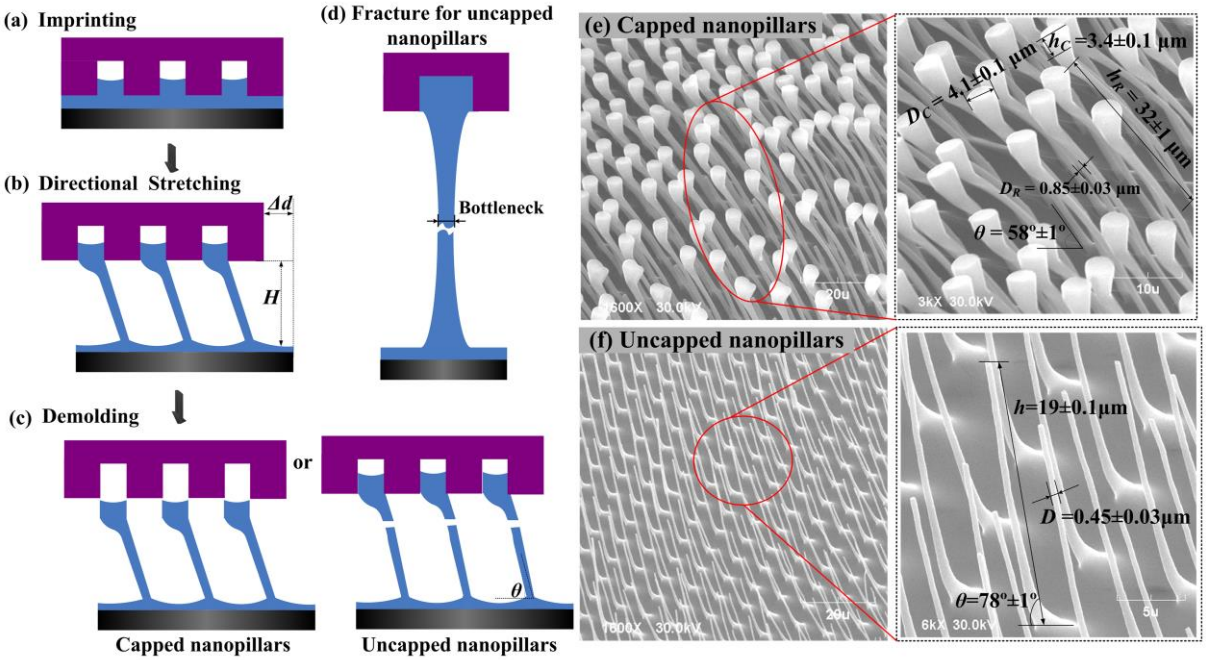

Fig. 1. Fabrication of high-aspect-ratio nanopillars. (a)-(c): Scheme of stretching nanoimprint for slanted and capped/uncapped nanopillars; (d) the formation of uncapped nanopillars, by fracture in the middle (bottleneck) of the stretching filament, left both nanopillars on substrate and mold, more details in Fig. S1; (e) the capped nanopillars and (f) uncapped nanopillars by the proposed stretching imprint process. It can be found that, both the capped and uncapped nanopillars have high aspect ratio, up to 40, and a controllable slanted angle.

The standing high-aspect-ratio nanopillars are fabricated on thermal plastic materials (i.e., PMMA) by a strecthing nanoimprint process with a microstructured mold (the microstructures on the mold are microholes array). **Fig. 1** outlines the fabrication scheme. Compared to conventional thermal nanoimprint process, there were two different aspects in the process needing to notify: (a) the temperature we employed is beyond polymer's melting point, that $T > T_M$, rather than $T > T_g$ in thermal nanoimprint; (b) the demolding experienced a large temperature range, from above T_M to room temperature (20 ˚C) by a controlling temperature decrease. So, during demolding, PMMA undergoes visco-elastic and plastic states as temperature drops [25]. At the end of demolding, there are two situations may occur: (a) the stretching ends by fracture in the middle of the filament, thus uncapped nanopillars were obtained (Fig. 1(c)); (b) the adopted mold completely detached from PMMA patterns, and left capped nanopillars on substrate (Fig. 1(d)). Which situation would finally occur is determined by temperature, stretching velocity, and also the interfacial energies of the adopted polymeric materials (i.e., PMMA) and the mold. Fig. 1 (e) and (f) show the two typical structures after demolding. It is observed that, in both situations, we can obtain nanopillars with up to 40 in aspect ratio. In addition, slanted nanopillars can be also prepared by a controllable offset demolding, as Fig. 1(b) shows, and the slanted angle can be depicted as $\varphi = \arctan(H / \Delta d)$, where Δd is the horizontal offset when demolding. In our experiments, the slanted angle obtained can be ranging from 60° - 90°.

It should be noticed that, for the capped nanopillars shown by Fig. 1 (e), the cap profile is dependent on that of the mold cavity, with the same linewidth. The height of the cap, however, is lower than that of mold cavity, which implies the probable deformation along the pillar stretching. The potential stretching also indicated that, during the detachment from mold, the cap slides along the cavity wall, and finally peeled off. Interestingly, when demolding starts from 175℃ (the melting point of PMMA is 165℃), capped nanopillars are prone to occur when slowly demolding (demolding speed is 1-3 mm/s), with diameters in 850±30 nm. In contrast, nanopillars without cap tend to occur when faster demolding (demolding speed is 3-5 mm/s), and the final pillar is around 450±30 nm in diameter. The demolding velocity dependence of the obtained diameters can attribute to the polymer evolution when demolding. For fast demolding, the stretching mainly occurs in the melting state (before detachment from the mold) of PMMA, in which visco-elastic behavior dominates, and the viscosity and cohesive force is much lower, thus the stretched structures are prone to be slender and fracture during stretching, forming slender nanopillars without cap (in this case, the potential cap is trapped in the mold cavity, as **Fig. S1(a)** shows). We found that there were also nanopillars existing on the mold, and their distribution perfectly matches the prepared uncapped nanopillar on substrate.

For the capped nanopillars, the demolding process actually can be divided into 2 stages. At first stage, the replicated pattern was stretched along the demolding direction when PMMA lies in its visco-elastic state ($T_g<T<T_M$). At second stage ($T \leqslant T_g$), PMMA is solidified, and mold detaches from the nanopillar, instead of stretching. The two-stage demolding process can be verified by

the profile of final cap, which takes the same linewidth as that of the mold cavity, as well as the observation of the mold after demolding, which contains no PMMA in the cavity (as Fig. S1(b) shows).

From Fig. 1 (e) and (f), it is obviously that, high-aspect-ratio (up to 40) and slanted nanopillars can be controllably prepared by a micro-featured mold. In our experiments, we always asked ourselves the question of what the smallest diameter and highest aspect ratio we can achieve by the simple stretching method. We found that, the smallest diameter and highest aspect ratio we can achieve were dependent on the stretching process (related to temperature, demolding velocity, etc.), the interfacial energies of polymeric materials and the mold, as well as the cavity profile of the adopted mold. The stretching process involves complicated polymer rheology at different temperature and the mechanical confinement of micro-featured mold, and it deserves further investigation. In our experiments, for PMMA, we achieved the nanopillars of 450nm in diameter and 40 in aspect ratio.

It should be noted that, the nanostructures obtained by the proposed stretching nanoimprint process is essentially determined by the filament evolution of the adopted materials during stretching, in which the viscosity of the adopted materials plays an important role [26]. Thus, the proposed stretching nanoimprint process is not only valid for the thermal-plastic materials (stretching around their melting temperature, the viscosity can be controlled by temperature), but also for the UV curable materials (stretching at the partial-cured stage [27], the viscosity can be controlled by the curing time). In our experiments, several thermal-plastic materials, i.e., PMMA, Poly(acrylic acid) (PAA), polyvinyl alcohol (PVA, 17-88), were successfully adopted to obtain high-aspect-ratio nanopillars, as well as a UV curable material (LT-2730, Lactite, as Figure S2 shows). The filament evolution during the dynamic stretching process can be found in previous studies [26, 28].

When engineering a functional surface bearing nanopillars with high aspect ratios, one should consider the stability of the expected structures. There are several factors that can lead to the collapse of vertical-standing nanopillars: collapse due to self-weight, due to adhesion force between the pillars and the base surface, and due to lateral adhesion between the pillars themselves. Roca-Cusachs et al. [29] suggested that at smaller dimensions, (sub)micrometer regime, adhesion between the pillar and the substrate and between the pillars themselves dominates over gravity and becomes the main cause for ground collapse or lateral collapse of the micro/nano pillars.

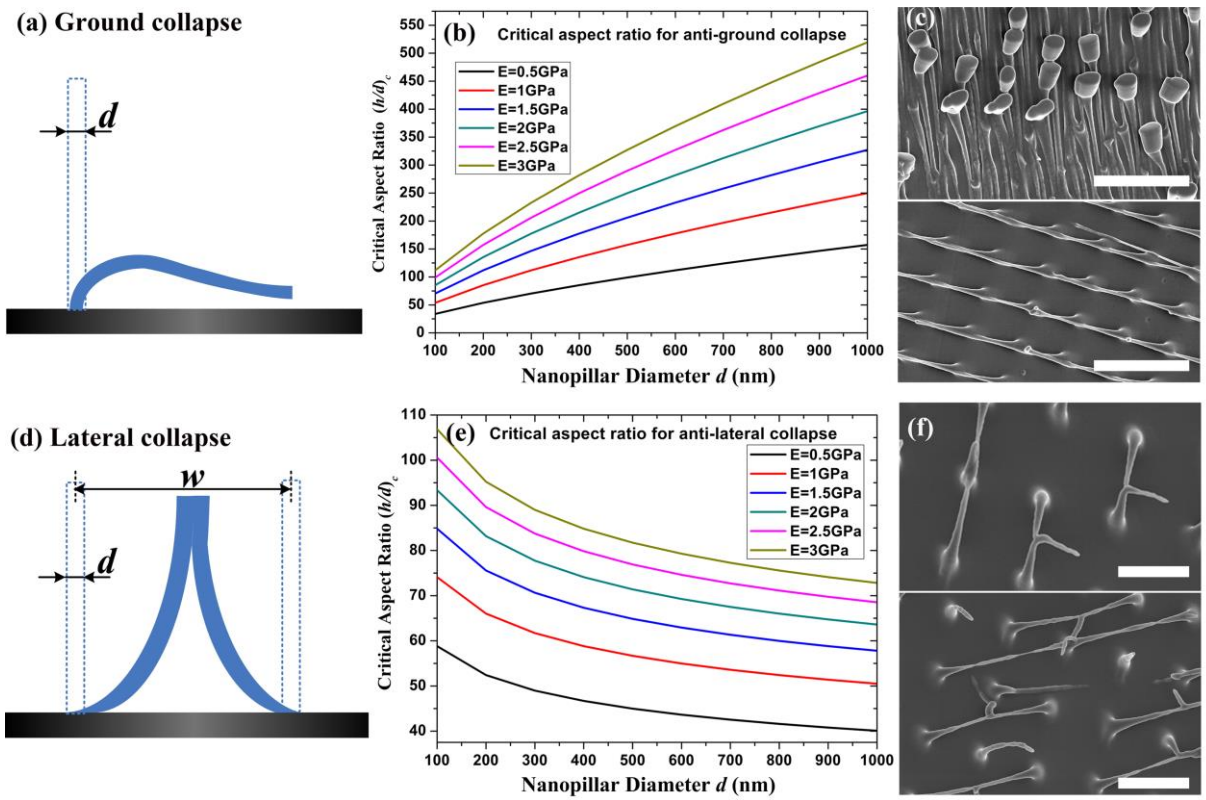

Fig. 2. The illustration of ground collapse (a) and lateral collapse (d). The theoretical study of the critical aspect ratio for (b) anti-ground collapse and (e) anti-lateral collapse. (c) The ground collapse and (f) lateral collapse found in our experiments due to the unoptimized demolding. It is obviously that, for the lateral collapse, the tips of the adjacent nanopillars merged together, rather than stick to each other observed in other studies, which indicates that the collapse occur at a high temperature, may above T*g*. All scale bars in (c) and (f) are 5μm.

For ground collapse, as **Fig. 2**(a) shows, by balancing the bending energy of the ground collapsed micropillar with the energy of pillar adhesion to the substrate, the criterion for critical aspect ratio, $(h/d)_c$, is [29]

$$\left(\frac{h}{d}\right)_c = \frac{\pi^{5/3}}{2^{11/3}3^{1/2}}(1-\nu^2)^{-1/6}\left(\frac{E}{2\gamma_{SV}}\right)^{2/3} d^{2/3} \quad (1)$$

where h is the height, d is the pillar diameter, E is Young's modulus, ν is Poisson ratio, and γ_{SV} is the surface energy of the pillar material.

The lateral collapse, as Fig. 2(d) shows, is more dominant for high density nanopillars. Aizenberg et al [30], Yang et al [31], and Duan et al [32] introduced capillary force to the well-designed high-aspect-ratio micro/nano pillars by making these structures susceptible to deformation and clustering. By balancing the bending energy and the energy of deformation (to make adhesion over a finite area) of laterally adhered pillars with their energy of adhesion, Glassmarker et al. [33] derived expressions for the critical aspect ratio against lateral collapse for pillars with circular cross-section, as Equation (2) shows.

$$\left(\frac{h}{d}\right)_c = \left(\frac{3^{3/4}\pi E w^{3/2}}{2^{1/4}32\gamma_{SV}(1-\nu^2)^{1/4}d^{1/2}}\right)^{1/3} \quad (2)$$

where w is the lateral separation between adjacent micropillars.

For a given micropillar array geometry, Equation 1 and 2 can be rearranged to obtain a critical moludlus, E_c (E_{c-g} for ground collapse, and E_{c-l} for lateral collapse), below which the pillars are unstable, as Fig. 2 (b) and (e) show. For the nanopillars shown in Fig. 1 (e) and (f), i.e., d = 850 nm, h = 32 μm and aspect ratio AR= 37.6 for the capped nanopillar, and d=450 nm, h=19μm, AR= 42.2 for the uncapped nanopillar, E_{c-g} estimated by Equation (1) is about 68 MPa and 154 MPa , E_{c-l} estimated by Equation (2) is about 382 MPa and 392 MPa, smaller than the modulus of PMMA at room temperature (normally 2000-3000 MPa).

It is well known that, the modulus of amorphous polymers is temperature dependent, and it decreases very rapidly falling by several orders of magnitude over a small temperature range in the glass-rubber transition region (around T_g) [34]. In our experiments, however, the fabrication process experiences a large temperature range, from T_M to room temperature. As temperature dissipates, the PMMA modulus increases from a few Pa to 2000-3000 MPa (at room temperature) [35]. Thus, the PMMA nanopillars may collapse during the demolding, depending on the match of demolding velocity and the cooling speed.

Fig. 2 (c) and (f) show the prepared structures by unmatched demolding velocity and cooling speed. Compared to Fig. 1 (e) and (f), the structures shown in Fig. 2 (c) and (f) were prepared at a lower cooling speed, which induce a smaller modulus of the nanopillars not stiff enough to against collapse. For the uncapped nanopillars in Fig. 2 (f), it clearly that, lateral collapse occurs, the tips of adjacent pillars, however, merge together, rather than stick to each other as other studies reported [30-32]. The merging tips indicate that, the lateral collapse happens above T_g, which can attribute to the slow cooling.

Interestingly, at room temperature, although the standing PMMA nanopillars have a large modulus, up to 2400 MPa, they can be actuated to deform reversibly by electron beam irradiation, or even by an external electric field, which is favorable when designing functional nanostructured materials for applications in actuation/sensing.

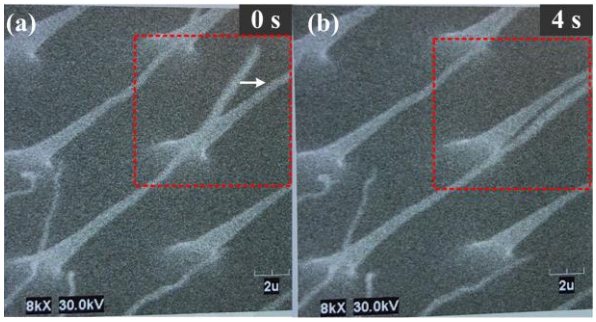

Fig. 3. Actuation of the nanopillars made by PMMA. (a) E-beam illumination starts; (b).E-beam illumination lasts for 4 s.

E-beam-induced nanopillar bending was investigated by Aizenberg et al. [28], and the bending is believed that due to the electron implanting as a result of backscattering, as well as the electrostatic force and torques due to the charging and induction. In our experiments, the prepared high-aspect-ratio nanopillars can be also actuated by electron beam when placed in a scanning electron microscope, as **Fig. 3** and **Video S1** show. Compared to the studies by Aizenberg et al. [35], it should be noted that: (a) in our experiments, although in a nanopillar matrix, the nanopillar was driven individually, instead of bending toward the center of the scanning window; (b) the deflection of each nanopillar can be up to over 10 μm. The asymmetry bending and larger deflection may attribute to the higher aspect ratio and the slanted angle. The bending in our experiments can be also recovered when decreasing the beam energies.

More interestingly, our experiments show that, the high-aspect-ratio nanopillars (made by PMMA, as a dielectric material) can swing in an AC electric field, whose deflection can be over 10 μm, as **Video S2** shows. Such large moving range is very promising for nanostructures, especially for such "stiff" PMMA material with modulus about 2.4 GPa. It well known that, the directional slanted angle of the nanopillars plays a key role in the anisotropic adhesion property. Gecko-like high-aspect-ratio, angled nanostructures take various fascinating features [33], while they are difficult to create. Thus, the actuation of the hight-aspect-ratio, angled nanopillars, in which the slanted angle can be dynamic tuned by external electric field, would be more promising for bioinspired reversible adhesion.

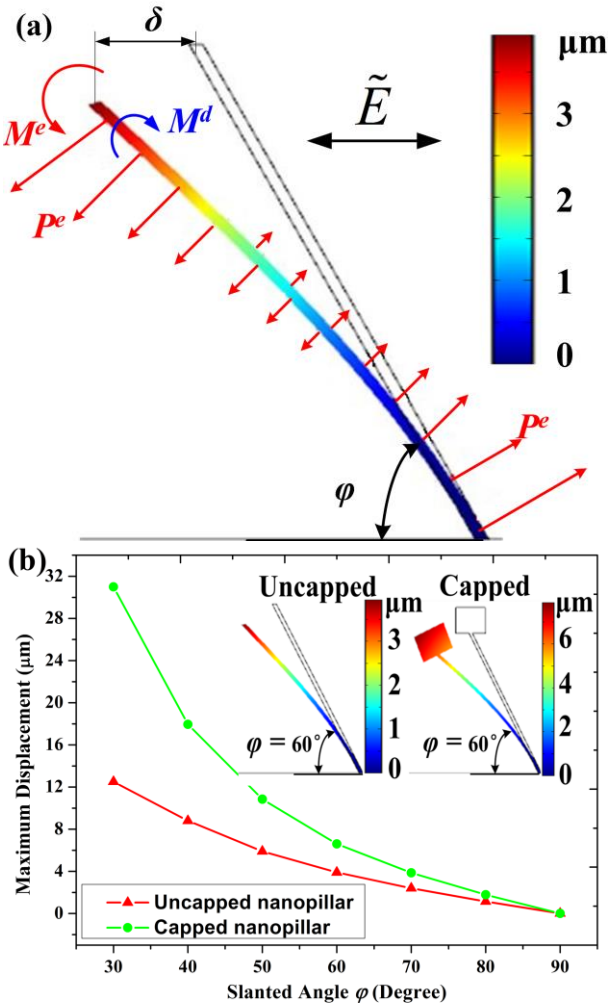

Fig. 4. Actuation of the directional high-aspect-ratio nanopillars by AC electric field (). (a) the driven mechanism by electric field. P^e is the electrical pressure exerted on the nanopillar by electric field, which induces an anti-clockwise torque (M^e) to drive the pillar rotating counter-clockwisely. When the pillar deforms, the internal stress is against the rotation, resulting in a anti-rotating torque, M^d. The rotation of the nanopillar is dominated by the two torques, M^e and M^d. (b) Comparison of the deflections of the capped and uncapped nanopillars. Obviously capped nanopillars tend to much larger deflection when driven.

As **Fig. 4**(a) shows, in an electric field, for a dielectric material, a Maxwell stress tensor, T^e, is produced at the air/polymer interface with an expression as follow:

$$T^e = \varepsilon_i \boldsymbol{E}_i \boldsymbol{E}_i - \frac{1}{2} E_i^2 [\varepsilon - \rho_i (\frac{\partial \varepsilon_i}{\partial \rho_i})] \boldsymbol{I} \quad (3)$$

Where ε_0 is the permittivity of the free space, ε_i is the relative permittivity of the air or polymer, E_i is the electric intensity on the air or the polymeric nanopillar, and ρ_i is the mass density of the air or polymer. Here, 'i' represents the air by 'a' or the polymer by 'p'.

The Maxwell stress tensor can result in an electrical pressure (P^e) at the air/polymer interface to drive the bending of the polymeric nanorod, which can be expressed as

$$P^e = T_a^e \cdot n + T_p^e \cdot n = -\frac{1}{2} \varepsilon_0 \varepsilon_p (\varepsilon_p - 1)^2 E_p^2 \quad (4)$$

where n is a unit normal pointing outward from polymer to air. In detail, the electric field in air produces an electrical pressure at the air-polymer interface pointing into the air, and that on the polymer domain generates a pressure at the interface pointing into the polymer. The resultant pressure between the two electrical pressures can generate the deformation of the polymeric nanopillars with the direction of pointing outward to air, resulting in an anti-clockwise torque, M^e , and driving the anti-clockwise rotation of the nanopillar.

While the nanopillar anti-clockwisely rotates and deviates its initial position, the internal stress increases and induces a clockwise torque, M^d , against the offset driving torque M^e . Thus, the nanopillar can swing under the cooperation of these two torques induced by an AC electric field. **Video S3** shows the swinging velocity of the nanopillar in an electric field by simulation, indicating the dynamic balancing of the two torques. It should be noted that, the maximum deflection in simulation is at the same scale as that in experiments (Video S2), indicating the validation of simulations.

The capped and uncapped nanopillars, as Fig. 1 (e) and (f) shows, act differently in electric field. The actuation of each kind of nanopillars was investigated in our experiemts. For the capped nanopillars, the nanopillars can swing dramatically in electric field, with over 10 μm in amplitude,. In contrast, the uncapped nanopillars can be also actuated by electric field, while with much smaller swing amplitude.

Fig. 4 (b) compares the maximum deflection of the two kinds of nanopillars, both are 480 nm in diameter and 40 in aspect ratio, while one has a 4μm-width, 3μm-height cap. Apparently, (a) slanted angle plays a key role in the actuation, the nanopillars with more offset from vertical-stand state (that is, smaller slanted angle) is preferred to actuation, which may explained by the slanted angle dependence of the effective modulus [36]; (b) the capped nanopillar is easier to be actuated, which can attribute to the probable accumulation of electric field along the cap edge, as well as the potential structural instability due to the cap.

It is well known that, modulus plays a key role for nanopillars stability, and also for their actuation. Higher modulus is preferred to stability, but against actuation ability. So, it is necessary to investigate the actuation ability of the nanopillars at different modulus, in the present of stability, i.e., anti- ground and lateral collapse. Fig. 5(a) shows the actuation ability of uncapped nanopillars at modulus ranging from 800-3000MPa. It should be noted that, (a) for ideally upright nanopillar ($\varphi = 90°$), the swing in electric field is less than 1 μm in amplitude, due to the symmetry electric force in both sides; (b) slanted angle is favorable to actuation, while modulus is heavily adverse to actuation. Further investigation of modulus dependence of actuation, as Fig. 5(b) shows, the swing amplitude, namely the max deflection of the pillars, is proportional to inverse modulus, E^{-1}, which can be explained to the pillar deflection under exerted force. When the force F acts along the entire post length l, perpendicular to the posts, the deflection δ , at a given point l_z from the base, is given by [37]:

$$\delta = F l_z^3 / 8EI \propto E^{-1} \quad (4)$$

where E is the modulus and I is moment of inertia.

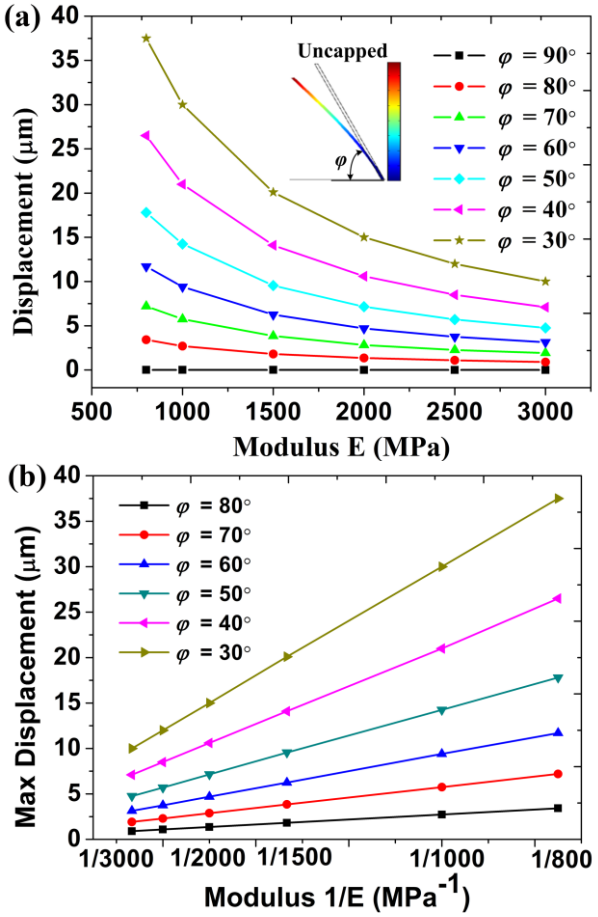

Fig. 5 (a) the slanted angle and (b) modulus dependence of the actuation.

In conclusion, arrays of directional high-aspect-ratio nanopillars (submicron in diameter and >40 in aspect ratio), can be fabricated by an unconventional imprint process with microstructured mold. Both capped and uncapped nanopillars with controlled slanted angles can be prepared by carefully processing control. Although the nanopillars are made by PMMA with high modulus of 2.4 GPa, they can undergo strong swinging in response to an AC electric field, with a maximum deflection of over 10 μm. Both experiments and simulation show that, slanted capped nanopillars is preferred to actuation. Our approach demonstrates an effective way to prepare directional high-aspect-ratio nanopillars which can be strongly bending in response to a external stimuli. The high aspect ratio nanopillars with orientation tunability can find applications in development of smart material, gecko-inspired reversible adhesion, etc.

Experimental Detail

Nanopillars Fabrication: The imprint mold is made of Teflon, with microholes array on it (4 μm in diameter and 1.5 in aspect ratio). The patterned polymer is Poly (methyl methacrylate), (PMMA, Mw=1.2×105, Tg =105℃, TM =165℃) dissolved in toluene (10 wt%). For molding, cleaned glass substrates were spin-coated at 3000rpm for 20s with a 10 wt% PMMA solution in toluene to the thickness of 20 μm. The Teflon mold was placed on the polymer surface under a slight pressure (~ 10^3 Pa) to make conformal contact, and the temperature was raised above TM (typically at 175 ℃) for 5-6 hours. For demolding, the temperature was first adjusted to the target demolding temperature in the range of 105℃-175℃, and during demolding, the temperature dropped to room temperature in a control manner. The mold was removed in a vertical direction while with a controlled horizontal offset from original position at a constant speed (which was varied from 1 mm/s to 10 mm/s in our study).

Nanopillars actuation: For the actuation by electron beam, the prepared samples with nanopillars were then sputter-coated with a 5-10 nm layer of gold, placed in SEM and grounded. Imaging was performed with a Cable 9000C (Japan) e-beam lithography system. When nanopillars were imaged for a few seconds under the e-beam at high magnification, the bending was recorded by a digital camera videoing on the screener.

For the actuation by electric field, two electrodes (copper tape, with copper thickness over 50 μm, larger than the nanopillar height) were paralleled placed, with a distance about 0.8 mm. Square-waved voltage was supplied by a function/arbitrary-waveform generator (AGILENTER 33220A) which was bridged with amplifier/controller (TREK 610E H.V.), with an amplitude of 1000 V and frequency of 20 Hz. In the simulation, the AC field was set the same as the actuation experiments. The swing of nanopillar was observed and recorded by using a KEYENCE VH-8000 microscope at 1000× magnification.

Acknowledgements

This research was financed by Natural Science Foundation of China (No. 91323303, 51305337 and No. 51275400). The authors also acknowledge the Research Fund for the Doctoral Program of Higher Education of China (No. 20130201120036), the China Postdoctoral Science Foundation (No. 2012M520081, 2013M530419, 2013M530424, and 2013M532035) and the Natural Science Foundation of Shaanxi Province (2013JQ7021).

Notes and references

State Key Laboratory for Manufacturing Systems Engineering, Xi'an Jiaotong University, Xi'an 710049, China. Fax: 86-29-83399508; Tel: 86-29-83399525; E-mail: hzliu@mail.xjtu.edu.cn, wtjiang@mail.xjtu.edu.cn

† Electronic Supplementary Information (ESI) available: [Fig. S1, Fig. S2, Video S1, Video S2, Video S3]. See DOI: 10.1039/b000000x/

1. P. J. Glazer, J. Leuven, H. An, S. G. Lemay, E. Mendes. *Adv. Funct. Mater.* **2013**, *23*, 2964-2970.
2. N. Hirokawa , Y. Tanaka , Y. Okada , S. Takeda , *Cell*, **2006**, *125* , 33-45.
3. K. Liu, L. Jiang, *Annu. Rev. Mater. Res.* **2012**, 42, 231-263.
4. A. I. Neto, H. J. Meredith, C. L. Jenkins, J. J. Wilker, J. F. Mano, *RSC Adv*, **2013**, 3, 935-9356.
5. W. Jiang, H. Liu, L. Wang, S. Zhu, L. Yin, Y. Shi, B. Chen, Y. Ding, N. An. *Thin Solid Films*, **2014**, 562, 383-388.
6. Z. G. Zhou , Z. W. Liu , *J. Bionic. Eng.* **2008** , *5* , 358-365.
7. L. D. Zarzar , P. Kim , J. Aizenberg , *Adv. Mater*. **2011** , *23* , 1442-1446.
8. F. Liu , D. Ramachandran , M. W. Urban , *Adv. Funct. Mater.* **2010** , *20* , 3163-3167.
9. O. Tabata , H. Hirasawa , S. Aoki , R. Yoshida , E. Kokufuta , *Sens. Actuators. A*, **2002** , *95* , 234-238.
10. D. Chandra , J. A. Taylor , S. Yang , *Soft Matter* . **2008** , *4* , 979-984.
11. A. Sidorenko , T. Krupenkin , A. Taylor , P. Fratzl , J. Aizenberg , *Science*. **2007** , *315* , 487-490.

12. T. Watanabe , M. Akiyama , K. Totani , S. M. Kuebler , F. Stellacci , W. Wenseleers , K. Braun , S. R. Marder , J. W. Perry , *Adv. Funct. Mater*. **2002** , *12* , 611-614.
13. E. W. H. Jager , E. Smela , O. Inganas , *Science* **2000** , *290* , 1540-1545.
14. J. le Digabel , N. Biais , J. Fresnais , J. F. Berret , P. Hersen , B. Ladoux , *Lab Chip* **2011** , *11* , 2630-2636.
15. B. A. Evans , A. R. Shields , R. L. Carroll , S. Washburn , M. R. Falvo , R. Superfi ne , *Nano Lett.* **2007** , *7* , 1428-1434.
16. B. Porkroy, , A.K. Epstein, M.C.M. Persson-Gulda, J. Aizenberg. **2009**, *Adv. Mater*, *21*, 463-469.
17. J. Aizenberg, V. C. Sundar, A. D. Yablon, J. C. Weaver, G. Chen, Proc. *Natl. Acad. Sci. U.S.A.* **2004**, *101*, 3358-3363.
18. V. C. Sundar, A. D. Yablon, J. L. Grazul, M. Ilan, J. Aizenberg, *Nature* **2003**, *424*, 899-890.
19. M. J. McHenry, S. M. van Netten, *J. Exp. Biol*. **2007**, *210*, 4244-4253.
20. E. E. Ruppert, R. S. Fox, R. B. Barnes, Invertebrate Zoology, Brooks Cole Thomson, Belmont, CA, U.S.A **2004**.
21. A. Sidorenko, T. Krupenkin, A. Taylor, P. Fratzl, J. Aizenberg, *Science* **2007**, *315*, 487-490
22. S. Vogel, Life's Devices: the physical world of animals and plants, Princeton University Press, Princeton, NJ, **1988**.
23. S. Nishimoto, B. Bhushan. *RSC Adv*. **2013**, 3, 671-690.
24. S.Tawfick, M. De Volder, D. Copic, S. J. Park, C. R. Oliver, E. S. Polsen, M. J. Roberts, A. J. Hart. *Adv. Mater*. **2012**, *24*, 1628-1674.
25. A. Chenevirere, E. Drockenmuller, D. Damiron, F. Cousin, F. Boue, F. Restagno, L. Leger, *Macromolecules*, **2013**, *46*, 6955-6922.
26. G.H. McKinley, T. Sridhar. *Annua. Rev. Fluid. Mech*. **2002**, *34*, 375-415.
27. W. Jiang, Y. Ding, H. Liu, B. Lu, Y. Shi, J. Shao, L. Yin. *Microelectron. Eng*. **2008**, *85*, 458-464.
28. M. Yao, G.H. McKinley, B. Debbaut. *J. Non-Newtonian Fluid Mech.* **1998**, *79*, 469-501.
29. P. Roca-Cusachs, F. Rico, E. Martinez, J. Toset, R. Farre, and D. Navajas. *Langmiur*, **2005**, *21*, 5542-5548.
30. B. Pokroy, S.H., Kang, L. Mahadevan, J. Aizenberg. *Science*, **2009**, *323*, 237-240.
31. D. Chandra, S. Yang. *Acc. Chem. Res.*. **2010**, *43*, 1080-1091.
32. H. Duan, K.K. Berggren. *Nano Lett*. **2010**, *10*, 3710-3716.
33. N.J. Glassmarker, A. Jagota, C.Y. Kim. *J. R. Soc. Interface*, **2004**, *1*, 23-33.
34. N. Lagakos, J. Jarzynski, J.H. Cole, J.A. Bucaro. *J. Appl. Phys*. **1986**, *59*, 4017-4031.
35. A. Seminara, B. Pokroy, S.H. Kang, M.P. Brenner, J. Aizenberg. *Phys. Rev. B*. 83, **2011**, 235438.
36. K. Autumn, C. Majidi, R.E. Groff, A. Dittmore, R. Fearing. *J. Exp. Bio*. **2006**, *209*, 3558-3568.
37. A. R. Ragab, S.E.A. Bayoumi, *Engineering Solid Mechanics: Fundamentals and Applications*, CRC Press, Boca Raton, FL, USA, **1998**.